

# Single-cell label-free photoacoustic flowoxigraphy in vivo

Lidai Wang, Konstantin Maslov, and Lihong V. Wang<sup>1</sup>

Optical Imaging Laboratory, Department of Biomedical Engineering, Washington University in St. Louis, St. Louis, MO 63130

Edited\* by Rakesh K. Jain, Harvard Medical School and Massachusetts General Hospital, Boston, MA, and approved February 27, 2013 (received for review September 10, 2012)

**Label-free functional imaging of single red blood cells (RBCs) in vivo holds the key to uncovering the fundamental mechanism of oxygen metabolism in cells. To this end, we developed single-RBC photoacoustic flowoxigraphy (FOG), which can image oxygen delivery from single flowing RBCs in vivo with millisecond-scale temporal resolution and micrometer-scale spatial resolution. Using intrinsic optical absorption contrast from oxyhemoglobin (HbO<sub>2</sub>) and deoxyhemoglobin (HbR), FOG allows label-free imaging. Multiple single-RBC functional parameters, including total hemoglobin concentration (C<sub>Hb</sub>), oxygen saturation (sO<sub>2</sub>), sO<sub>2</sub> gradient (∇sO<sub>2</sub>), flow speed (v<sub>f</sub>), and oxygen release rate (rO<sub>2</sub>), have been quantified simultaneously in real time. Working in reflection instead of transmission mode, the system allows minimally invasive imaging at more anatomical sites. We showed the capability to measure relationships among sO<sub>2</sub>, ∇sO<sub>2</sub>, v<sub>f</sub>, and rO<sub>2</sub> in a living mouse brain. We also demonstrated that single-RBC oxygen delivery was modulated by changing either the inhalation gas or blood glucose. Furthermore, we showed that the coupling between neural activity and oxygen delivery could be imaged at the single-RBC level in the brain. The single-RBC functional imaging capability of FOG enables numerous biomedical studies and clinical applications.**

photoacoustic microscopy | flow cytometry | oximetry | oxygenation | microenvironment

Most living cells require oxygen to metabolize nutrients into usable energy. In vivo imaging of oxygen transport and consumption at high spatial and temporal resolution is required to understand the metabolism of cells and their related functionalities. Although individual parameters such as oxygen saturation (sO<sub>2</sub>) (1, 2), partial oxygen pressure (pO<sub>2</sub>) (3, 4), or blood flow speed (v<sub>f</sub>) (4–7) may partially indicate tissue oxygenation, none of them can provide a complete description of oxygen transport. To quantify tissue oxygenation in vivo, three primary imaging modalities have been applied: positron emission tomography (PET) (8), functional magnetic resonance imaging (fMRI) (9, 10), and diffuse optical tomography (DOT) (11). Although these methods may provide deep functional imaging, they all suffer from millimeter-scale spatial resolutions. Recently, photoacoustic (PA) microscopy was proposed to measure the oxygen metabolic rate at feeding and draining blood vessels (12). However, the assessment is limited to a relatively large region; moreover, the feeding and draining blood vessels—especially those surrounding a tumor—may be numerous and difficult to identify. Because micrometer-sized RBCs are the basic elements for delivering most of the oxygen to cells and tissues, the need for direct imaging of oxygen release from flowing single RBCs in vivo is imperative. A molecular imaging method based on the measurement of ground-state recovery time has been investigated for hemoglobin sensing (13), but in vivo measurement of oxygen saturation has not been implemented. Dual-wavelength spectrophotometry has been applied to measure oxygen release for decades (14), but transmission-mode imaging limits its application to very thin tissue. Many biomedical problems—for example, tumor or neuroscience studies—require minimally invasive imaging at various anatomical sites. A new method for in vivo imaging of single-RBC oxygen release in reflection mode will enable many in vivo

studies of fundamental oxygen transport and of oxygenation-related tissue functionalities and critical diseases.

We developed single-RBC PA flowoxigraphy (FOG) (12, 15–18), which allows label-free real-time reflection-mode imaging of single flowing RBCs delivering oxygen to tissue in vivo. The single-RBC FOG is based on high-resolution functional PA microscopy (Fig. 1) (12, 15–18). Several innovations were made to enable real-time spectral imaging of single flowing RBCs. Two synchronized lasers are used to periodically generate two laser pulses 20 μs apart at 532 nm (an isosbestic wavelength of hemoglobin) and 560 nm (a nonisosbestic wavelength). At each beam position, two laser pulses sequentially excite nearly the same region of a cell to acquire two depth-resolved PA signals (A-lines), which are used to spectrally detect the relative concentrations of HbO<sub>2</sub> and HbR. Then, we readily can calculate the sO<sub>2</sub> and relative hemoglobin concentration (C<sub>Hb</sub>). To quantify the local oxygen delivery, the average hemoglobin concentration <C<sub>Hb</sub>> is computed by averaging C<sub>Hb</sub> over the field of view. <C<sub>Hb</sub>> is proportional to the hematocrit. However, measurement of the <C<sub>Hb</sub>> in absolute units remains a challenge because of the difficulty in determining local fluence in vivo. The PA probe is mounted onto a fast voice-coil linear scanner to enable real-time imaging. Because the B-scan rate is fast enough to image single RBCs flowing through the field of view, flow speed is computed from the cross-correlation between two consecutive B-scan images acquired at 532 nm. The oxygen release rate (rO<sub>2</sub>) can be determined from the following equation (12, 17):

$$rO_2 = k \times \langle C_{Hb} \rangle \times \nabla sO_2 \times v_f, \quad [1]$$

where *k* is a constant coefficient related to the hemoglobin oxygen-binding capacity. Note that ∇sO<sub>2</sub>, v<sub>f</sub>, and rO<sub>2</sub> represent averages over the field of view.

FOG has achieved a micrometer-scale spatial resolution, >100-Hz 2D imaging speed, and 20-μs oxygenation detection time. Moreover, this device can simultaneously quantify the relative C<sub>Hb</sub>, sO<sub>2</sub>, ∇sO<sub>2</sub>, v<sub>f</sub>, and rO<sub>2</sub>, where the ∇sO<sub>2</sub> is defined as the sO<sub>2</sub> reduction per unit distance along the flow. Because the gradient vector of single-RBC sO<sub>2</sub> always points upstream, we use ∇sO<sub>2</sub> to represent the amplitude of the gradient only. Sensing intrinsic optical absorption contrast from HbO<sub>2</sub> and HbR, the single-RBC FOG allows label-free imaging.

Using single-RBC FOG, we imaged dynamic oxygen release from single RBCs in vivo. First, single-RBC oxygen deliveries were imaged in the mouse brain. By simultaneously measuring multiple functional parameters, we demonstrated the capability to measure the relationship among sO<sub>2</sub>, ∇sO<sub>2</sub>, v<sub>f</sub>, and rO<sub>2</sub>. Then, we imaged

Author contributions: L.W., K.M., and L.V.W. designed research; L.W. performed research; L.W. analyzed data; and L.W. and L.V.W. wrote the paper.

The authors declare no conflict of interest.

\*This Direct Submission article had a prearranged editor.

Conflict of interest statement: L.V.W. has a financial interest in Microphotoacoustics, Inc. and Endra, Inc., which, however, did not support this work. K.M. has a financial interest in Microphotoacoustics, Inc., which also did not support this work.

<sup>1</sup>To whom correspondence should be addressed. E-mail: lhwang@seas.wustl.edu.

This article contains supporting information online at [www.pnas.org/lookup/suppl/doi:10.1073/pnas.1215578110/-DCSupplemental](http://www.pnas.org/lookup/suppl/doi:10.1073/pnas.1215578110/-DCSupplemental).

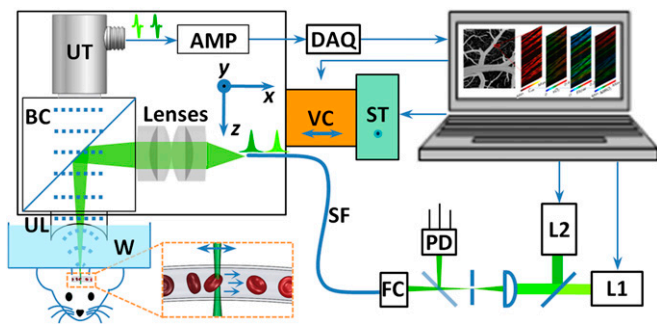


**Fig. 1.** Schematic of single-RBC FOG. AMP, signal amplifiers and filters; BC, acoustic-optical beam combiner; DAQ, digitizer; FC, fiber coupler; L1, pulsed laser 1, 560 nm; L2, pulsed laser 2, 532 nm; Lenses, two achromatic doublets; PD, photodiode; SF, single-mode fiber; ST, stepper motor scanner ( $y$ -axis); UL, ultrasound lens; UT, ultrasound transducer; VC, voice-coil scanner ( $x$ -axis); W, water.

single-RBC oxygen deliveries under two challenges: altering inhalation gas from low to high oxygen concentration and inducing acute hypoglycemia. We observed that oxygen deliveries were modulated in both cases. Next, neuron–RBC coupling in the brain was imaged. Experimental results showed a strong correlation between neural stimulus and single-RBC oxygen delivery and demonstrated a unique approach to studying brain functions at the single-RBC level.

## Results

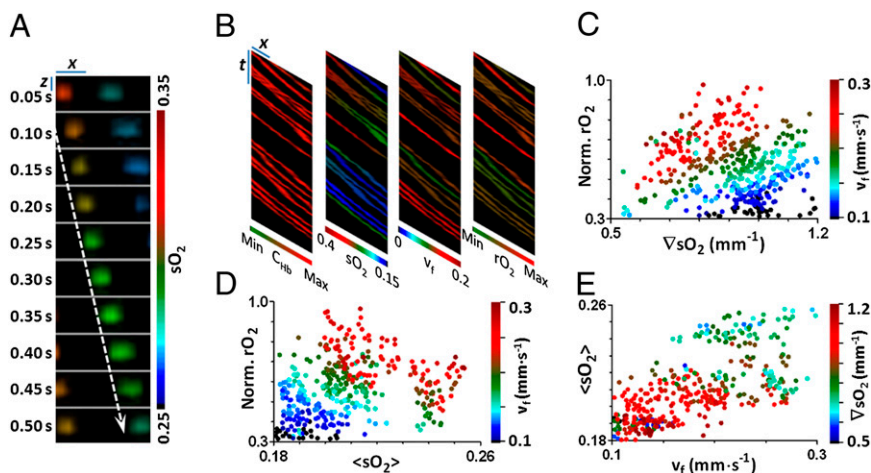
### Quantitative Measurement of Oxygen Release from Single RBCs in Vivo.

To record real-time oxygen delivery, a set of B-scan images was acquired at varied time points (Fig. 2A), as single RBCs flowed from the left to the right side of the field of view. A real-time video is shown in [Movie S1](#). The oxygen release from single RBCs was clearly imaged cell by cell. A representative RBC shown in Fig. 2A desaturated by 0.03 over a 32- $\mu\text{m}$  travel distance. The oxygenation imaging speed currently is limited by the 2-kHz pulse repetition rate of the 560-nm pulsed laser, which may be improved in the future to enable 3D single-RBC FOG. Taking advantage of the ultra-short wavelength switching time, fast scanning speed, and high spatial resolution, we can simultaneously quantify  $C_{\text{Hb}}$ ,  $s\text{O}_2$ ,  $\nabla s\text{O}_2$ ,  $v_f$ , and

$r\text{O}_2$  from images of single RBCs, as shown in Fig. 2B. By operating a 532-nm single-wavelength laser at a 20-kHz pulse repetition rate, we achieved 3D imaging of flowing single RBCs with a 20-Hz rate, as shown in [Movie S2](#).

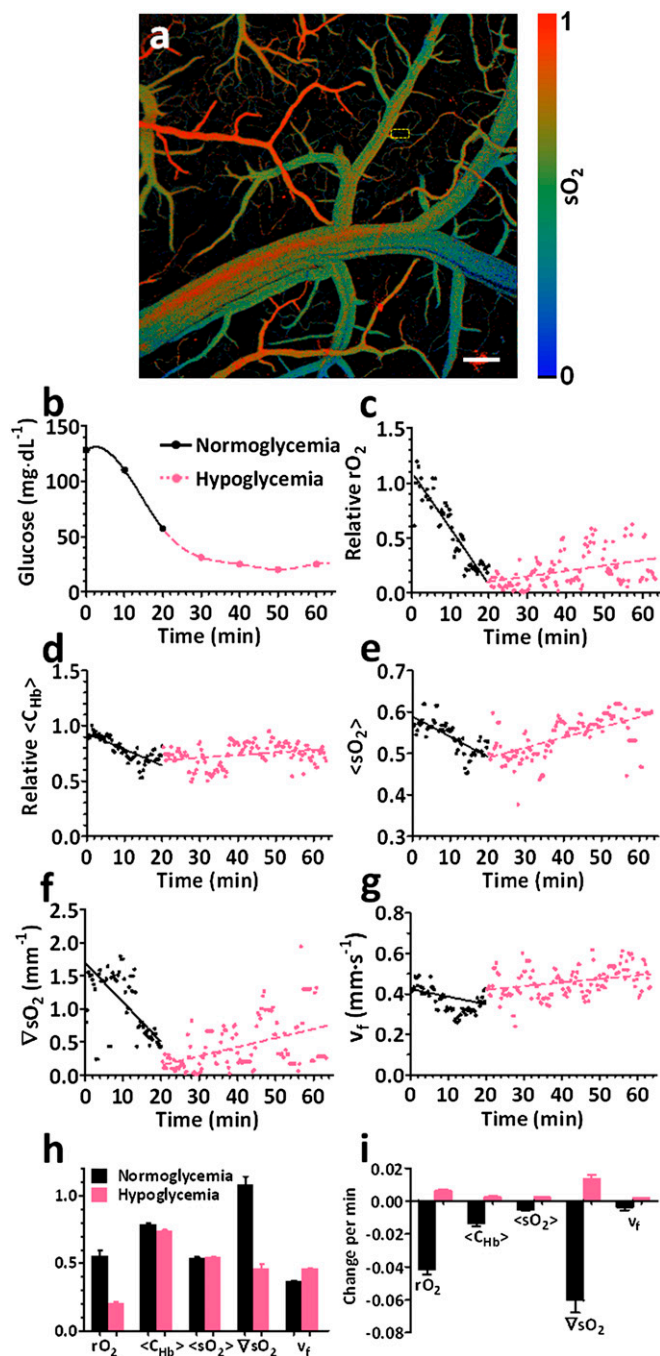
**Relationship Among Single-RBC Parameters.** FOG has the capability to measure relationships among multiple parameters of a single RBC. Here, we imaged single flowing RBCs in designated vessels in the mouse brain cortex at a 20-Hz B-scan rate while the mice were breathing air mixed with isoflurane. The imaged flowing RBCs were 60–150  $\mu\text{m}$  deep from the brain cortex surface and had travel distances of 30–60  $\mu\text{m}$  within the B-scan window. The vessel inclination was less than  $20^\circ$  with respect to the  $x$ - $y$  plane. More than 6,000 B-scan images were acquired at each wavelength. We simultaneously calculated multiple functional parameters from the single-RBC images and averaged every 20 B-scans. Even without applying any challenge or stimulation, oxygen delivery was found to fluctuate. Although RBC oxygen saturation should be relatively uniform in arterioles, we observed dramatic  $s\text{O}_2$  variations from cell to cell in some vessels. A plausible reason for the variations is that the imaged vessel segment was close to venules and the RBCs released different amounts of oxygen before they were imaged. We further imaged  $s\text{O}_2$  variations in different segments of capillaries. The  $s\text{O}_2$  of capillaries close to the arterial end had an average SD of  $0.09 \pm 0.03$ . The  $s\text{O}_2$  of capillaries close to the venous end had an average SD of  $0.12 \pm 0.04$ . Each SD first was calculated from 500 measurements in a capillary, then was averaged over 30 capillaries. A  $t$  test showed that the arterial end had a smaller SD than the venous end with  $P < 0.01$ .

Fig. 2C–E shows the relationships among  $\langle s\text{O}_2 \rangle$ ,  $\nabla s\text{O}_2$ ,  $v_f$ , and  $r\text{O}_2$ . As expected from Eq. 1, Fig. 2C shows that  $r\text{O}_2$  increases with both  $\nabla s\text{O}_2$  and  $v_f$ . Whereas the former reflects the amount of oxygen released by each RBC, the latter determines the dwell time of flowing RBCs in the field of view. Fig. 2D shows that increasing  $v_f$  increases  $r\text{O}_2$  if  $\langle s\text{O}_2 \rangle$  is maintained constant, but increasing  $\langle s\text{O}_2 \rangle$  decreases  $r\text{O}_2$  if  $v_f$  is held constant. From Fig. 2C and D, we also observed that for constant  $r\text{O}_2$ , increasing  $v_f$  decreases  $\nabla s\text{O}_2$  and increases  $\langle s\text{O}_2 \rangle$ . Fig. 2E shows that a decrease of either  $v_f$  or  $\langle s\text{O}_2 \rangle$  is correlated with increasing  $\nabla s\text{O}_2$ . Taken from another set of data, [Fig. S1](#) and [Movies S3](#) and [S4](#)



**Fig. 2.** (A) Sequential snapshots ([Movie S1](#)) of single RBCs releasing oxygen in a mouse brain. Scale bars:  $x = 10 \mu\text{m}$ ,  $z = 30 \mu\text{m}$ . Blood flows from left to right. The dashed arrow follows the trajectory of a single flowing RBC. (B) Simultaneous measurement of multiple parameters from the images of single RBCs, including relative total hemoglobin concentration ( $C_{\text{Hb}}$ ), oxygen saturation ( $s\text{O}_2$ ), flow speed ( $v_f$ , in millimeters per second $^{-1}$ ), and relative oxygen release rate ( $r\text{O}_2$ ). At each time  $t$ , the 1D image along the  $x$ -axis shows the maximum amplitude projection (MAP) along the  $z$ -axis. Each oblique line in the  $x$ - $t$  images tracks one RBC. Scale bars:  $x = 10 \mu\text{m}$ ,  $t = 1$  s. (C) Normalized  $r\text{O}_2$  vs.  $\nabla s\text{O}_2$  at varied  $v_f$ . (D) Normalized  $r\text{O}_2$  vs.  $\langle s\text{O}_2 \rangle$  at varied  $v_f$ , where  $\langle s\text{O}_2 \rangle$  denotes the  $s\text{O}_2$  averaged over the RBC travel distance in the field of view. (E)  $\langle s\text{O}_2 \rangle$  vs.  $v_f$  at varied  $\nabla s\text{O}_2$ . In C–E, each point represents one measurement averaged over 1 s.





**Fig. 4.** (A) Representative  $sO_2$  MAP image of the mouse brain cortex. Scale bar: 200  $\mu\text{m}$ . (B) Systemic blood glucose levels measured every 10 min after insulin injection. Interpolation was performed to obtain a continuous curve. (C–G)  $rO_2$ ,  $\langle C_{Hb} \rangle$ ,  $\langle sO_2 \rangle$ ,  $\nabla sO_2$ , and  $v_f$  quantified from single-RBC images. (H) Comparison of the averages between normoglycemia and hypoglycemia. Error bars are SEM. (I) Comparison of the fitted slopes between normoglycemia and hypoglycemia. Error bars are SD.

Swiss Webster mouse. Target RBCs were imaged in the right visual cortex region of the brain through a craniotomy. Fig. 5B shows the transient responses of single RBCs to single visual stimulations (a 0.5-s flash). Each parameter first was computed from images of single RBCs, then averaged over 1 s for 104 trials. Statistical analyses based on four mice showed that  $\langle sO_2 \rangle$ ,  $\nabla sO_2$ ,  $v_f$ , and  $rO_2$  changed significantly after visual stimulation, but  $\langle C_{Hb} \rangle$  did not show obvious changes. We observed an increase in flow speed after

stimulation, reaching its peak 4–10 s after initial stimulation. The single-RBC  $\langle sO_2 \rangle$  exhibited a biphasic response: it remained unchanged within 3–5 s after stimulation, then proceeded to rise, and peaked after 8–10 s. The response of  $\nabla sO_2$  and  $rO_2$  also showed behaviors similar to that of  $\langle sO_2 \rangle$ .

The coupling between neurons and single RBCs also was imaged under continuous visual stimulation by flashing the LED light at 1 Hz. Single RBCs in the visual cortex region were imaged at 20–100 Hz, depending on the blood flow speed. Fig. 5C and D show representative  $sO_2$  images acquired without and with continuous visual stimulation, respectively. The  $\langle sO_2 \rangle$  decreased under continuous visual stimulation. We also measured the  $rO_2$  while alternating the continuous visual stimulus on and off, as shown in Movie S6. All single-RBC parameters, including  $\langle C_{Hb} \rangle$ ,  $\langle sO_2 \rangle$ ,  $\nabla sO_2$ ,  $v_f$ , and  $rO_2$ , were compared without and with continuous visual stimulation. Each of the parameters was normalized to its mean value computed from the data without stimulation and plotted in Fig. 5E. Experimental results from three mice show that  $\langle C_{Hb} \rangle$  did not change significantly, the  $\langle sO_2 \rangle$  decreased by  $4 \pm 0.8\%$ , and the  $\nabla sO_2$ ,  $v_f$ , and  $rO_2$  increased by  $53 \pm 6\%$ ,  $8 \pm 1\%$ , and  $56 \pm 9\%$ , respectively.

With the single-RBC resolution, we further quantified the probability distributions of the single-RBC parameters. Fig. 5F–I shows the cumulative distribution functions (CDFs) of the significantly changed parameters. With continuous stimulation, the single-RBC functions exhibited distributions different from those in the control experiment, i.e., lower  $\langle sO_2 \rangle$  and higher  $\nabla sO_2$ ,  $v_f$ , and  $rO_2$ , consistent with the data shown in Fig. 5E.

## Discussion

The experimental results demonstrate that single-RBC FOG is an effective tool for in vivo imaging of oxygen release from single RBCs. The micrometer-scale lateral spatial resolution and the >100-Hz 2D imaging rate enable resolution of single flowing RBCs in real time. The short (20- $\mu\text{s}$ ) dual-wavelength switching time enables the detection of oxygenation in flowing RBCs. During fast scanning, this imaging modality maintains the confocal alignment between the optical and acoustic foci. This alignment provides signal-to-noise ratio (SNR) superior to that of optical scanning (18, 24) and is of great importance for sensitive functional imaging. Single-RBC FOG also has the advantage of label-free imaging, relying on intrinsic optical absorption contrast from HbO<sub>2</sub> and HbR. This feature avoids the use of contrast agents that might be chemically toxic, phototoxic, radioactive, or disruptive to the imaging targets. As in many other in vivo measurement methods, FOG also might perturb in vivo oxygen release from RBCs. However, this effect was mitigated by both label-free imaging and low-energy excitation. Taking full advantage of single-RBC FOG, we directly imaged the dynamic processes of single RBCs delivering oxygen to local cells and tissues in vivo at multiple anatomical sites, including the brain.

Single-RBC FOG can simultaneously measure multiple parameters, including  $C_{Hb}$ ,  $sO_2$ ,  $\nabla sO_2$ ,  $v_f$ , and  $rO_2$ . Such a capability may uncover the relationships between these tightly related parameters and provide a comprehensive view of cell and tissue oxygenation with high spatiotemporal resolution. We imaged the dynamics of single-RBC oxygen release during a transition of inhalation gas from low to high oxygen, as well as during an acute blood glucose decrease. We observed that RBC oxygen release changed in both cases. Unlike high-resolution imaging of  $pO_2$  (3, 4), single-RBC FOG measures the oxygen released, which quantifies tissue metabolism more directly than measurement of oxygen tension.

Using single-RBC FOG, we have shown the unique capability of measuring the coupling between neural activity and single-RBC oxygen delivery in the brain. We imaged the transient RBC responses evoked by single visual stimulation, where we observed a clear biphasic response of single-RBC  $\langle sO_2 \rangle$ . Under continuous visual stimulation, the average  $sO_2$  decreased. Single-RBC FOG can confine the detection of neurovascular coupling to the single-RBC level.

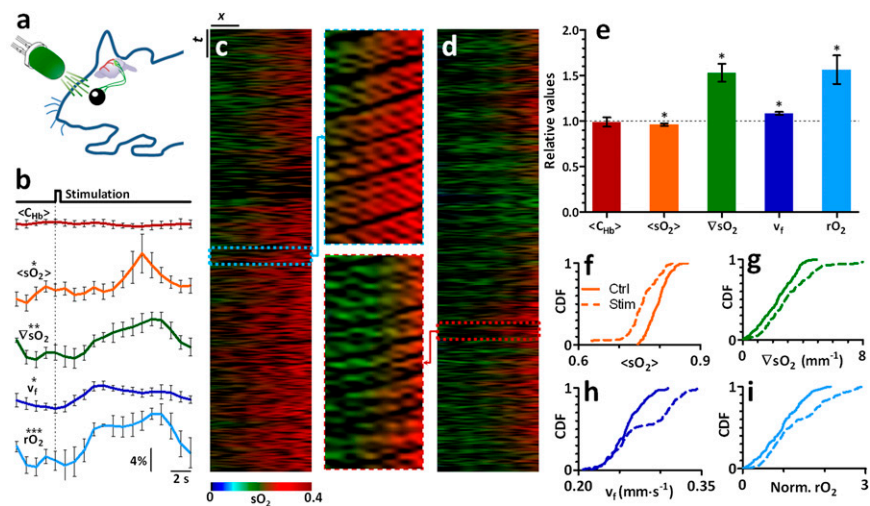


**Fig. 5.** Imaging of neuron–single-RBC coupling in mouse visual cortex. (A) Schematic of the experimental setup. (B) Transient responses to a single visual stimulation. The  $sO_2$ ,  $\nabla sO_2$ ,  $v_f$ , and  $rO_2$  have statistically significant changes according to two-way ANOVA tests ( $n = 4$ ). Error bars denote SEMs.  $*P < 0.05$ ,  $**P < 0.01$ ,  $***P < 0.001$ . (C) Representative MAP images without continuous visual stimulation. (D) Representative MAP images with 1-Hz continuous optical flashing stimulations on the left mouse eye. Scale bars in C and D:  $x = 10 \mu\text{m}$ ,  $t = 10 \text{s}$ . (E) Relative changes of single-RBC functional parameters under continuous visual stimulation. Values are normalized to mean values of control images. The  $\langle sO_2 \rangle$ ,  $\nabla sO_2$ ,  $v_f$ , and  $rO_2$  are significantly different from their control values according to two-way ANOVA tests ( $n = 3$ ). Error bars denote SEMs.  $*P < 0.05$ . (F–I) CDFs of  $\langle sO_2 \rangle$ ,  $\nabla sO_2$ ,  $v_f$ , and  $rO_2$  under control (ctrl) and stimulation (stim).  $rO_2$  was normalized to the mean value of the control experiment.

Single RBCs, as basic oxygen carriers, play a key role in oxygenating most cells and tissues. To date, the lack of technologies available for direct functional imaging of single RBCs in reflection mode *in vivo* has been a major limiting factor in studies of oxygen transport in the microenvironment at high temporal and spatial resolution. The single-RBC FOG demonstrated here has broken through this limitation by directly imaging the oxygen release from single RBCs, as well as allowing for simultaneous measurement of relative  $C_{Hb}$ ,  $sO_2$ ,  $\nabla sO_2$ ,  $v_f$ , and relative  $rO_2$ .

Through detection of oxygen delivery at the ultimate temporal and spatial resolution, single-cell FOG may bring benefits to many preclinical or clinical applications, such as tumor heterogeneity or microenvironment studies, the early diagnosis of tumor, monitoring of tumor treatment, and high-resolution brain functional imaging. The cell-by-cell statistics might shed additional light as well, although they require more study. This advance in single-RBC FOG has opened avenues for *in vivo* study of fundamental principles in tissue oxygenation and related diseases.

## Methods

**Experimental Setup.** Building on the basis of high-resolution functional PA microscopy (12, 15–18), several innovations enable real-time spectral imaging of single moving RBCs. Two lasers are used to periodically generate two laser pulses 20  $\mu\text{s}$  apart at 532 nm (an isosbestic wavelength of hemoglobin) and 560 nm (a nonisosbestic wavelength of hemoglobin), whose pulse widths are  $< 10 \text{ns}$ . Both lasers operate at a 2-kHz pulse repetition rate. The two laser beams are merged into a single-mode optical fiber, then delivered to a PA probe. For pulse-to-pulse calibration, the energy of each laser pulse is detected by a biased photodiode. The laser beam from the fiber is focused onto targets through a pair of optical lenses (N.A. in water: 0.1), an acoustic–optical beam combiner, and an ultrasound lens. The optical lenses may be adjusted to coalign the acoustic and optical foci accurately. The acoustic–optical beam combiner, which is composed of two prisms and a coated aluminum layer in the middle, reflects light but transmits sound (18). The tight optical focus provides a 3.4- $\mu\text{m}$  lateral spatial resolution (18), which was quantified by imaging a sharp edge in water and deriving the line spread function. Laser-excited PA waves are collected by the ultrasound lens, transmitted through the acoustic–optical beam combiner, and detected by a high-frequency ultrasound transducer (V214; Olympus NDT; 50 MHz central frequency). The PA signals are amplified, filtered, and digitized at 500 MHz. The ultrasound transducer provides an axial resolution of 15  $\mu\text{m}$ , as determined from a shift-and-sum method (25). A maximum imaging depth of 1.2 mm was demonstrated in a living mouse

(18). For single-RBC functional imaging, FOG reached a depth of 308  $\mu\text{m}$ , as shown in Fig. S2. Because of light scattering and absorption in tissue, the imaging sensitivity changes with depth. Accurate measurement of hemoglobin concentration and oxygen release rate in absolute units remains a challenge for *in vivo* imaging. Here, we studied only the relative change of hemoglobin concentration and the relative oxygen release rate.

At each position, two laser pulses sequentially excite nearly the same region of the target to acquire two depth-resolved PA signals (A-lines). Taking a flow speed of 10  $\text{mm}\cdot\text{s}^{-1}$  as an example, the target moves 0.2  $\mu\text{m}$  during the wavelength switching, which is much smaller than the spatial resolution and thus is negligible. Because  $\text{HbO}_2$  and  $\text{HbR}$  have molar extinction coefficients with different spectral characteristics, and PA signals are linearly related to the concentrations of  $\text{HbO}_2$  and  $\text{HbR}$  at low-excitation laser energy [ $< 100 \text{nJ}$  per pulse (12)], the relative concentrations of  $\text{HbO}_2$  and  $\text{HbR}$  may be computed from the PA signals (1, 16) of the same RBC excited at 532 nm and 560 nm. From the  $\text{HbO}_2$  and  $\text{HbR}$  concentrations, we can calculate the relative  $C_{Hb}$  and  $sO_2$  of single RBCs.

The PA probe is mounted onto a fast voice-coil linear scanner to enable acquisition of at least 100 cross-sectional (B-scan) images per second. Mechanically scanning the entire PA probe maintains the acoustic–optical confocal alignment and therefore achieves higher SNR than pure optical scanning in a fixed acoustic focus (18, 24). A field-programmable gate array card (PCI-7830R; National Instrument) was programmed to synchronize the trigger signals and motion control commands. By fast scanning the PA probe along RBC flowing direction, we can image single RBCs flowing through the field of view, as well as directly measure the amount of oxygen bound to each RBC.

**Experimental Animals and Approved Protocols.** The ears of nude mice (Hsd: Athymic Nude-Fox1<sup>NU</sup>; Harlan Co.; 4–6 wk old, 20–25 g) and the brains of white mice (Hsd:ND4 Swiss Webster; Harlan Co., 4–6 wk old; 20–25 g) were imaged for all *in vivo* studies. During imaging, mice were placed on top of a 37  $^{\circ}\text{C}$  heating pad, secured with a head holder, and anesthetized with isoflurane [Isothesia (Isoflurane USP); Butler Schein Animal Health Supply]. Ultrasound gel was applied between the imaging areas and the water tank. After the ear imaging experiments, the mice recovered naturally. Brain imaging experiments were studied through a small craniotomy. After the brain imaging experiments, the mice were killed via cervical dislocation under deep anesthesia. The laser pulse energy used for the brain imaging usually was 40–50 nJ, but up to 100 nJ when deep RBCs were imaged. To offset skin attenuation, 80 nJ was used when the mouse ear was imaged. Note that the current experimental setup can image microvessel segments within a small angle ( $< 10^{\circ}$ ) from the voice-coil scanning axis ( $x$ -axis). For capillaries outside the angular range, either the scanner or the animal was rotated to reduce the angle. All experimental animal protocols were approved by the Animal Studies Committee at Washington University in St. Louis.

**ACKNOWLEDGMENTS.** The authors thank Feng Gao for discussion on statistics; Arie Krumholz, Sandra Matteucci, Seema Mukhi Dahlheimer, and James Ballard for manuscript editing; and Arie Krumholz, Dakang Yao, Junjie

Yao, and Song Hu for helpful discussions. This work was sponsored in part by National Institutes of Health Grants R01 EB000712, R43 HL106855, R01 EB008085, R01 CA134539, U54 CA136398, R01 CA157277, and R01 EB010049.

1. Zhang HF, Maslov K, Stoica G, Wang LV (2006) Functional photoacoustic microscopy for high-resolution and noninvasive in vivo imaging. *Nat Biotechnol* 24(7):848–851.
2. Millikan G (1942) The oximeter, an instrument for measuring continuously the oxygen saturation of arterial blood in man. *Rev Sci Instrum* 13(10):434.
3. Sakadžić S, et al. (2010) Two-photon high-resolution measurement of partial pressure of oxygen in cerebral vasculature and tissue. *Nat Methods* 7(9):755–759.
4. Lecoq J, et al. (2011) Simultaneous two-photon imaging of oxygen and blood flow in deep cerebral vessels. *Nat Med* 17(7):893–898.
5. Macé E, et al. (2011) Functional ultrasound imaging of the brain. *Nat Methods* 8(8):662–664.
6. Kamoun WS, et al. (2010) Simultaneous measurement of RBC velocity, flux, hematocrit and shear rate in vascular networks. *Nat Methods* 7(8):655–660.
7. Chaigneau E, Oheim M, Audinat E, Charpak S (2003) Two-photon imaging of capillary blood flow in olfactory bulb glomeruli. *Proc Natl Acad Sci USA* 100(22):13081–13086.
8. Frackowiak RSJ, Lenzi G-L, Jones T, Heather JD (1980) Quantitative measurement of regional cerebral blood flow and oxygen metabolism in man using <sup>15</sup>O and positron emission tomography: Theory, procedure, and normal values. *J Comput Assist Tomogr* 4(6):727–736.
9. Ogawa S, Lee TM, Kay AR, Tank DW (1990) Brain magnetic resonance imaging with contrast dependent on blood oxygenation. *Proc Natl Acad Sci USA* 87(24):9868–9872.
10. Logothetis NK, Guggenberger H, Peled S, Pauls J (1999) Functional imaging of the monkey brain. *Nat Neurosci* 2(6):555–562.
11. Culver JP, et al. (2003) Diffuse optical tomography of cerebral blood flow, oxygenation, and metabolism in rat during focal ischemia. *J Cereb Blood Flow Metab* 23(8):911–924.
12. Yao J, Maslov KI, Zhang Y, Xia Y, Wang LV (2011) Label-free oxygen-metabolic photoacoustic microscopy in vivo. *J Biomed Opt* 16(7):076003–076011.
13. Applegate BE, Izatt JA (2006) Molecular imaging of endogenous and exogenous chromophores using ground state recovery pump-probe optical coherence tomography. *Opt Express* 14(20):9142–9155.
14. Ellis CG, Ellsworth ML, Pittman RN (1990) Determination of red blood cell oxygenation in vivo by dual video densitometric image analysis. *Am J Physiol* 258(4 Pt 2):H1216–H1223.
15. Maslov K, Zhang HF, Hu S, Wang LV (2008) Optical-resolution photoacoustic microscopy for in vivo imaging of single capillaries. *Opt Lett* 33(9):929–931.
16. Hu S, Maslov K, Tsytarev V, Wang LV (2009) Functional transcranial brain imaging by optical-resolution photoacoustic microscopy. *J Biomed Opt* 14(4):040503.
17. Wang LV (2009) Multiscale photoacoustic microscopy and computed tomography. *Nat Photonics* 3(9):503–509.
18. Wang L, Maslov K, Yao J, Rao B, Wang LV (2011) Fast voice-coil scanning optical-resolution photoacoustic microscopy. *Opt Lett* 36(2):139–141.
19. Pitzer KR, et al. (2001) Detection of hypoglycemia with the Gluco Watch biographer. *Diabetes Care* 24(5):881–885.
20. Iadecola C (2004) Neurovascular regulation in the normal brain and in Alzheimer's disease. *Nat Rev Neurosci* 5(5):347–360.
21. Wu Z, et al. (2005) Role of the MEOX2 homeobox gene in neurovascular dysfunction in Alzheimer disease. *Nat Med* 11(9):959–965.
22. Zacchigna S, Lambrechts D, Carmeliet P (2008) Neurovascular signalling defects in neurodegeneration. *Nat Rev Neurosci* 9(3):169–181.
23. Mishra A, Hamid A, Newman EA (2011) Oxygen modulation of neurovascular coupling in the retina. *Proc Natl Acad Sci USA* 108(43):17827–17831.
24. Xie Z, Jiao S, Zhang HF, Puliafito CA (2009) Laser-scanning optical-resolution photoacoustic microscopy. *Opt Lett* 34(12):1771–1773.
25. Wang L, Maslov K, Xing W, Garcia-Urbe A, Wang LV (2012) Video-rate functional photoacoustic microscopy at depths. *J Biomed Opt* 17(10):106007.